Raman injection laser

Mariano Troccoli[1], **Alexey Belyanin**[2], **Federico Capasso**[1],
Ertugrul Cubukcu[1], **Deborah L. Sivco**[3] **& Alfred Y. Cho**[3]

[1]*Division of Engineering and Applied Sciences, Harvard University, Cambridge, Massachusetts 02138, USA*
[2]*Department of Physics, Texas A&M University, College Station, Texas 77843, USA*
[3]*Bell Laboratories, Lucent Technologies, Murray Hill, New Jersey 07974, USA*

....

Stimulated Raman scattering is a nonlinear optical process that, in a broad variety of materials, enables the generation of optical gain at a frequency that is shifted from that of the incident radiation by an amount corresponding to the frequency of an internal oscillation of the material[1,2]. This effect is the basis for a broad class of tunable sources known as Raman lasers[2,3]. In general, these sources have only small gain ($\sim 10^{-9}\,\mathrm{cm\,W^{-1}}$) and therefore require external pumping with powerful lasers, which limits their applications. Here we report the realization of a semiconductor injection Raman laser designed to circumvent these limitations. The physics underlying our device differs in a fundamental way from existing Raman lasers[3–8]: it is based on triply resonant stimulated Raman scattering between quantum-confined states within the active region of a quantum cascade laser that serves as an internal optical pump—the device is driven electrically and no external laser pump is required. This leads to an enhancement of orders of magnitude in the Raman gain, high conversion efficiency and low threshold. Our lasers combine the advantages of nonlinear optical devices and of semiconductor injection lasers, and could lead to a new class of compact and wavelength-agile mid-and far-infrared light sources.

In these electrical injection devices the Raman shift is determined by an electronic transition between quantum-well states, known as intersubband transitions (ISTs), rather than by a phonon energy as in conventional solid state Raman lasers, and as such can be designed over a broad range.

Very large resonant nonlinear optical susceptibilities of ISTs in semiconductor quantum wells have been demonstrated since the early 1990s[9,10]. Second harmonic generation with enhanced conversion efficiency has been reported in quantum cascade (QC) lasers using ISTs[11,12] and interband transitions[13]. Raman lasing using IST has been theoretically discussed[14] and observed experimentally in GaAs/AlGaAs double quantum wells optically pumped by a CO_2 laser[6,7]; the Raman shift was primarily determined by a phonon resonance, anticrossed with an IST. An important step towards major performance improvements was the recent demonstration of near-infrared Raman lasers, in which ultralow threshold was achieved thanks to the use of high-quality-factor (high-Q) dielectric microsphere resonators[8].

In a general scheme of the Raman process sketched in Fig. 1a, the internal oscillations in a medium correspond to the transition between states 1 and 2. The incident light of energy $\hbar\omega_L$ is converted into a signal of energy $\hbar\omega_S$, called Stokes radiation, where both frequencies are usually strongly detuned from other higher-lying states (that is, Δ is large compared to the broadening of level 3 in Fig. 1a) to avoid strong first-order absorption. In this case, only two-photon transitions between state 1 and 2 mediated by an intermediate virtual state may occur. As a result, the Raman gain resulting from the stimulated Raman scattering (SRS) process is of purely parametric origin as the energy of the Stokes beam is directly derived from the pump beam, that is, without intermediate storage in the medium[1].

In contrast, in resonant Raman lasing the pump and Stokes frequencies are near resonance with transitions 1–3 and 2–3 of the medium, and in turn coherently drive the transition at frequency

$\omega_{12} \approx \omega_L - \omega_S$. The triply resonant nature of this process enhances the stimulated Raman gain by many orders of magnitude with respect to the non-resonant case. In fact, the usual perturbative classification of nonlinear optical processes in powers of the electric field[1,2] breaks down, and the effect of the fundamental radiation needs to be taken into account exactly. In this situation, the nonlinear polarization becomes comparable in magnitude to the linear terms.
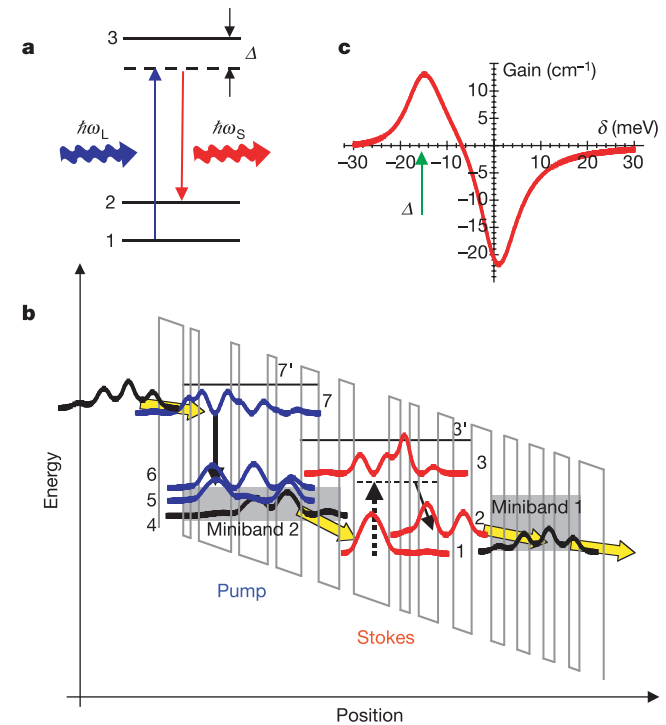
Figure 1 Diagrams showing the Raman effect and the band structure design. **a**, The Raman Stokes process. Solid and dashed lines indicate respectively real and virtual energy states. The fundamental excitation (blue), that is, the pump, is converted into a lower-energy radiation (red). Δ is the detuning of the incident radiation from the 1–3 transition resonance. **b**, Calculated conduction band structure of one period of the 30-stage Raman laser. The plot represents the potential profile along the growth direction, where the square moduli of only the most significant wavefunctions are indicated for clarity. The energy barriers (0.52 eV) are made of $Al_{0.48}In_{0.52}As$ and the quantum wells of $Ga_{0.47}In_{0.53}As$. Shown are the quantum cascade laser states (4, 5, 6, 7) and Raman region states (1, 2, 3). Two higher-lying states are indicated by straight lines (3′ and 7′), while the grey boxes indicate manifolds of closely spaced states (minibands 1 and 2). The layer thicknesses are (starting from the left, in nm): **4.2**, 1.3, **1.4**, 5.6, **1.4**, 4.9, **1.5**, 4.3, **3.0**, 3.6, **2.5**, 6.1, **2.0**, 1.6, **1.5**, 3.2, **2.6**, 3.2, **3.4**, 2.2, **2.3**, 2.1, **2.4**, 1.9, **2.5**, 1.8, **4.2**, where the barriers are indicated in boldface and the underlined layers are doped to $n = 4 \times 10^{17}\,\mathrm{cm^{-3}}$. The yellow arrows indicate the direction of electron transport. Electrons in the ground state of miniband 1 are injected by resonant tunnelling into the upper laser level (state 7) of the following period. The solid and dashed vertical arrows represent the internally generated pump laser radiation. The relevant calculated transition energies, dipole matrix elements and lifetimes are: $E_{76} = 186\,\mathrm{meV}$, $E_{65} = 31\,\mathrm{meV}$, $E_{54} = 39\,\mathrm{meV}$, $E_{32} = 150\,\mathrm{meV}$, $E_{31} = 199\,\mathrm{meV}$, $E_{21} = 49\,\mathrm{meV}$; $z_{32} = 1.31\,\mathrm{nm}$, $z_{31} = 1.23\,\mathrm{nm}$, $z_{21} = 0.7\,\mathrm{nm}$; $\tau_{32} = 4.5\,\mathrm{ps}$, $\tau_{31} = 1.9\,\mathrm{ps}$, $\tau_{21} = 5.4\,\mathrm{ps}$, $\tau_2 = 0.2\,\mathrm{ps}$, $\tau_3 = 0.4\,\mathrm{ps}$. The total broadenings of the transitions of the Raman section are estimated from absorption and electroluminescence data in the literature as: $\gamma_{32} = 5\,\mathrm{meV}$, $\gamma_{31} = 5\,\mathrm{meV}$, $\gamma_{21} = 4\,\mathrm{meV}$. **c**, Calculated Raman gain spectrum as a function of the detuning $\delta = \omega_S - \omega_{32}$. The detuning Δ of the pump laser field from the 3–1 transition is equal to 15 meV. The drive current used in the calculation corresponds to the threshold for Stokes lasing, so that the peak gain is very close to the estimated value for the waveguide losses at the Stokes wavelength. At the peak, corresponding to the two-photon resonance $\omega_S = \omega_L - \omega_{21}$, the two-photon (Raman) term in equation (1) exceeds the linear absorption term (proportional to $n_2 - n_3$) by more than a factor of 7.

In our injection-pumped resonant Raman laser, the fundamental and the Raman radiations are both generated by electronic transitions; these transitions are between confined states in the conduction band of the very same active region of a QC laser (Fig. 1b). Raman lasing is due to the excitation of a coherent electronic polarization on the mid-infrared IST between states 1 and 2. The resonant enhancement of the third order Raman susceptibility and the intra-cavity optical pumping scheme make the process very efficient (~30% power conversion). The intra-cavity pumping in each stage of the cascade overcomes the limitation of the exponential attenuation of the external pump in conventional Raman oscillators, so that the entire length of the cavity contributes to Raman lasing. Finally, the waveguide geometry ensures excellent mode overlap between the Raman and pump laser modes. The peak Raman gain coefficient per period can be estimated from the threshold condition for Stokes lasing: $\Gamma_S I_L N_P g_S = \alpha_w + \alpha_m$, where α_w, and α_m are respectively the waveguide and mirror losses at the Stokes frequency ($\alpha_w + \alpha_m = 11 \pm 3 \, \text{cm}^{-1}$), Γ_S is the fraction of the Stokes mode in the Raman section of the stack ($\Gamma_S \approx 0.15$), I_L is the internal pump laser intensity in the active region ($I_L = (3 \pm 0.5) \times 10^5 \, \text{W cm}^{-2}$), and N_P ($= 30$) is the number of active region periods. The Raman gain coefficient g_S is then $(8 \pm 3) \times 10^{-6} \, \text{cm W}^{-1}$.
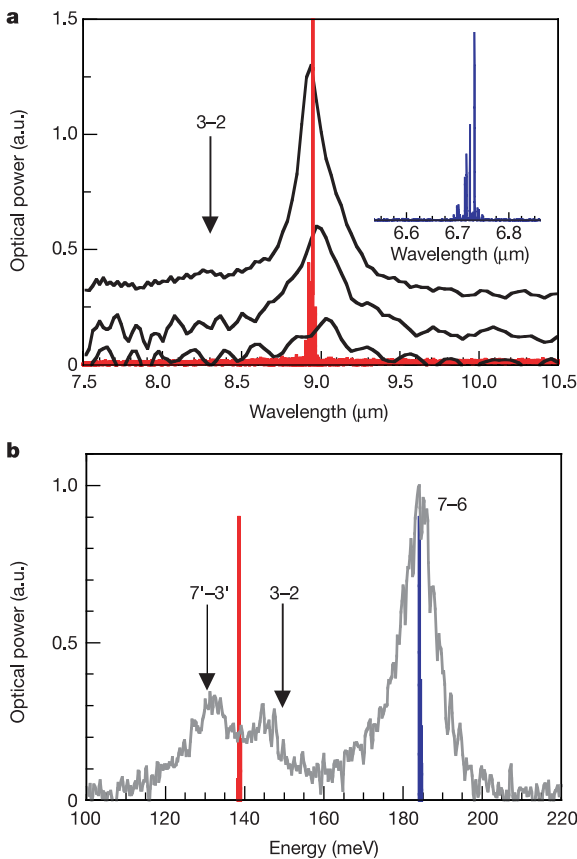
Figure 2 Spectral characteristics. **a**, Measured subthreshold emission spectra (black lines) of our QC Raman laser at currents of (from bottom to top) $I = 2.43$, 2.45 and 2.5 A, offset for clarity. The red curve is recorded above the threshold for Raman lasing ($I = 2.6$ A). Inset, fundamental laser emission spectrum at $I = 0.8$ A. The vertical arrow marks the position where the emission from the transition 3–2 would be expected if level 3 were populated by optical pumping. **b**, Comparison of electroluminescence (grey curve) and fundamental and Raman laser (blue and red curves, respectively) emission spectra. The vertical arrows indicate the energy of the transitions 3–2 and 7′–3′ as calculated from the band structure in Fig. 1b. All measurements were performed in pulsed operation at a heat sink temperature of $T = 80$ K with a repetition rate of 80 kHz and a pulse width of 100 ns.

In our design of the Raman laser, the typical layout of a QC laser has been carefully modified to include within the same band structure the Λ-scheme of three ISTs designed to produce SRS. Each period of the laser multistage structure consists of an injector, a pump region and a Stokes section where Raman lasing takes place (Fig. 1b).

The pump section consists of a coupled wells vertical transition active region[15], used in the design of state-of-the-art mid-infrared QC lasers[16], suitably modified for optimum coupling to the Stokes section. The pump is generated across the 7–6 transition, where state 6 is depleted by resonant optical-phonon emission to level 5. The energy of the 1–3 transition (E_{13}) is designed to be detuned by 13 meV from resonant absorption of the pump. Although the detuning lowers the gain, as is shown in equation (1) below, we kept it of the order of the 1–3 transition full-width at half-maximum, $2\gamma_{31} = 10$ meV, in order to decrease optical pumping to state 3 and to be able to distinguish between Raman lasing and usual lasing due to population inversion on the 3–2 transition.

Solution of the density matrix equations and of Maxwell's equations, in a more general treatment than the one already outlined in ref. 17, gives the following expression for the signal gain at the Stokes wavelength, in units of cm^{-1}:

$$g = \text{Re}\left\{ \frac{\eta}{\gamma_{32} + |\Omega_p|^2/(\gamma_{21} - i(\Delta - \delta)) + i\delta} \times \right.$$
$$\left. \left[\frac{|\Omega_p|^2(n_1 - n_3)}{(\gamma_{21} - i(\Delta - \delta))(\gamma_{31} - i\Delta)} - (n_2 - n_3) \right] \right\} \quad (1)$$

where $\Omega_p = e z_{13} E_p/\hbar$ is the Rabi frequency of the optical pump, E_p is its peak electric field, z_{13} is the dipole matrix element of the 1–3 transition and e is the electric charge, $n_{1,2,3}$ are the electron densities (per unit volume) of states 1,2,3, each γ is the total broadening (expressed as half-width at half-maximum, in frequency units) of the transition shown as a subscript, δ and Δ are the frequency detunings of the Raman and pump fields from the 3–2 and 3–1 transitions, respectively, and $\eta = 4\pi\omega_s e^2 z_{32}^2/\hbar c$. Note that the previously defined Raman gain coefficient g_S is related to the signal gain in equation (1) through the relation $g \approx g_S I_L$, because at the peak of the gain spectrum the absorption term in equation (1) is small. Equation (1) has been derived in the so-called rotating wave approximation, valid for small frequency detunings of the pump and Stokes fields from the relevant transitions, and assuming a constant, arbitrarily strong pump field. Many-body effects have also been neglected. This is justified for doping densities in the low $10^{11} \, \text{cm}^{-2}$ range typical of our structures, leading to a frequency shift of less than 1 meV, well below the typical broadening of any transition. The Rabi frequency, for an electric field averaged over the mode profile in the active region of $14 \, \text{kV cm}^{-1}$ (that is, at pump powers of 60 mW), corresponds to an energy of ~2 meV, comparable to the broadening of the relevant transitions ($\gamma \approx 4$–5 meV). It would be substantially larger in the case of more powerful QC lasers that reach up to 1 W. A formula equivalent to equation (1) has been obtained[18] for anti-Stokes amplification.

The gain according to equation (1) is plotted in Fig. 1c as a function of the Raman detuning δ for Δ corresponding to the band structure design. The two terms in square brackets in equation (1) demonstrate the competition between the one-photon absorption proportional to the population difference across the transition 3–2, and the nonlinear gain originating from the beating between the pump field and the off-diagonal element of the density matrix, that is, the so-called Raman coherence. In the limit when Δ becomes much larger than all linewidths, and one-photon processes are negligible, we recover from equation (1) the standard expression for the Raman gain proportional to $|E_p|^2(n_1 - n_2)/\Delta^2$.

As is clear from equation (1), the optimal band structure design

has to meet several conditions: (1) maximize the $z_{13} \times z_{32}$ product, included in $\eta \times |\Omega_p|^2$; (2) minimize $|z_{12}|^2$ to help maximize the $z_{13} \times z_{32}$ product because of a sum-rule argument; (3) minimize state 2 lifetime τ_2 and increase n_1 to maximize Raman inversion ($n_1 \gg n_2$); and (4) optimize the detuning $\Delta = E_{31} - E_{76}$. The resulting calculated band structure is shown in Fig. 1b. n-Type doping of the injector region alone ensures a large concentration of electrons in level 1, given that the latter lies only a few meV in energy above the lowest state of miniband 1, without causing an additional broadening of the states in the Stokes section. Specific values are given in Fig. 1 legend.
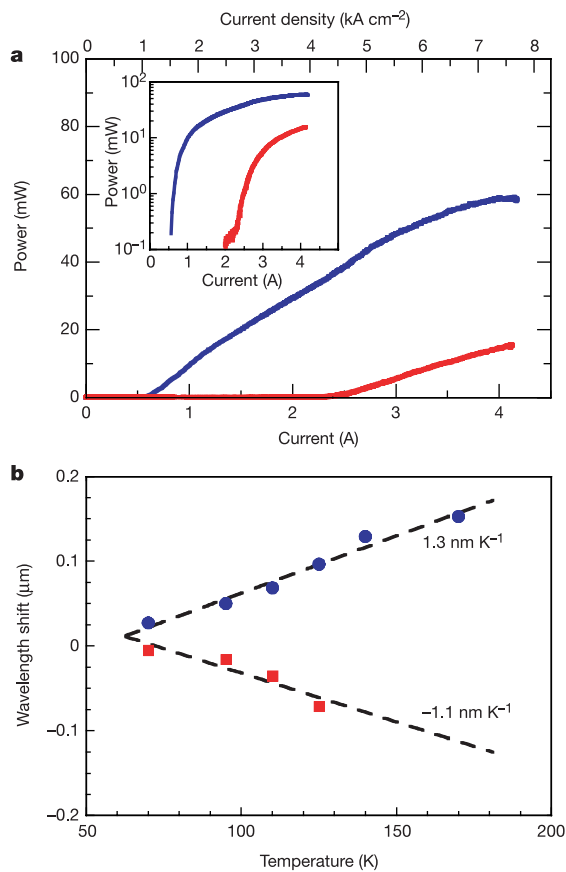
The devices were based on a InGaAs/InAlAs heterostructure, grown by molecular beam epitaxy and lattice-matched to the InP substrate. Typical emission spectra from ridge waveguide devices are shown in Fig. 2a. The pump wavelength (blue curve, inset) at a heat sink temperature of 80 K is measured to be $\lambda_L = 6.7\,\mu m$, corresponding very well to the predicted value of $\hbar\omega_L = 186\,meV = E_{76}$. The Stokes spectrum is peaked at a wavelength $\lambda_S = 8.9\,\mu m$, corresponding to the expected value $\hbar\omega_S = \hbar\omega_L - E_{21} = 137\,meV$, and its narrowing with increased current demonstrates that it is a SRS process. The onset of Raman lasing is observed above a threshold current of 2.6 A, as indicated by the appearance of narrow cavity modes centred near λ_S. Figure 2b shows the electroluminescence spectrum of the same material processed into round mesa devices (to prevent feedback from the facets and laser action) at the same current density ($J \approx 4.5\,kA\,cm^{-2}$) as that in laser devices at

Figure 3 Power output and temperature dependence. **a**, Peak output power versus current characteristics measured for the fundamental (blue) and Stokes (red) emission at a temperature of 80 K. Measurements were performed with a 5 kHz repetition rate at a 0.05% duty cycle. Inset, experimental power–current characteristics on a logarithmic scale, showing the exponential behaviour of the emission close to threshold. **b**, Wavelength shift with temperature of the pump (blue filled circles) and Raman laser emission (red filled squares) with respect to its value at 10 K. The opposite tuning with temperature of the Stokes emission is a signature of the two-photon resonance.

the threshold for Raman lasing. We can clearly identify the main peak as the pump transition E_{76}, while two low-intensity peaks appear at lower energies, neither of which corresponds to the Stokes emission. The spectral assignment of the observed features can be performed by a careful analysis of the band structure at the electric field corresponding to Raman lasing. The electric field at the threshold for Raman lasing is determined by measuring the voltage across the device and assuming that most of the voltage drop above threshold for current injection is in fact across the cladding layers, as previously demonstrated[19]. This leads to an estimated electric field of $51\,kV\,cm^{-1}$. The most intense electroluminescence peak is exactly centred at the pump laser photon energy, E_{76}, and the position of the Raman laser line is clearly distinguishable from the two minor peaks that we have assigned to the 7′–3′ and 3–2 transitions. This rules out the possibility that the Stokes line arises from conventional laser action between energy levels of the structure via electrical pumping. The upper states of these transitions are significantly detuned from the energy levels of the injector and of the active region but can still be weakly populated via hot electron effects and scattering, giving rise to the weak luminescence lines. Similarly, electroluminescence from transition 3–1 is expected to be weak and masked by the main luminescence peak.

The laser line at $\lambda \approx 9\,\mu m$ cannot arise from incoherent optical pumping of level 3, that is, our source cannot be confused with an optically pumped laser, because the 3–2 transition is completely out of resonance with the Stokes line (Fig. 2a).

Raman lasing was reproduced in all ten tested devices. The power output characteristics of a representative device are displayed in Fig. 3a. The measured samples exhibit typically two thresholds, the first one around $1\,kA\,cm^{-2}$, for the fundamental laser emission, and a second one around $4.3\,kA\,cm^{-2}$ for the Stokes emission. The two curves shown in Fig. 3a represent the laser emission turn-on of the fundamental (blue line) and Stokes (red line) radiation. The Stokes line turn-on occurs when the output laser power reaches about 40 mW, and at higher currents the Stokes power reaches about 26% of the fundamental power, where the fundamental emission starts to saturate, as commonly observed in QC lasers at injection levels of several times the threshold current. This should be compared to conversion efficiencies for solid-state Raman lasers that are usually very low ($\leq 10^{-3}$), with the exception of ultra-high-Q spherical microcavities ($\sim 20\%$) (ref. 8) and spin-flip Raman lasers in InSb ($\sim 50\%$) (ref. 2). Also shown in Fig. 3a are the emitted Stokes and fundamental output power as a function of current on a logarithmic scale, to highlight the exponential dependence of the emission below threshold as compared with the linear behaviour above threshold for both the laser lines. Given that the laser facets' reflectivity does not change significantly in the wavelength range $\lambda = 6$–$9\,\mu m$, we can consider the ratio of the emitted powers to be equal to the ratio of the internal power densities, measured by comparing the relative intensities of the laser peaks in spectra acquired over the entire mid-infrared range without any optical filtering. From these measurements, the conversion efficiency is estimated to be about 30% at currents of 4.5 A, in good agreement with the value obtained from the power–current curves.

The thermal behaviour of the devices also shows some peculiarities. Laser action is observed up to 170 K, whereas Stokes lasing appears up to 125 K in the range of currents explored. With a threshold current density parametrized as $J = J_0\exp(T/T_0)$, T_0 equals 97 K and 102 K for the pump and Stokes wavelengths, respectively. The emission wavelength shift with temperature is shown in Fig. 3b. The observed redshift for the pump laser is comparable to typical values for QC lasers, and amounts to $\Delta\lambda_L/\Delta T = 1.3\,nm\,K^{-1}$. In the case of the Raman line, there is a blueshift at increasing temperatures, $\Delta\lambda_S/\Delta T = -1.1\,nm\,K^{-1}$. This blueshift can be explained by recalling that the Stokes energy is given by $\hbar\omega_S = \hbar\omega_L - E_{21}$. Both $\hbar\omega_L$ and the Raman shift E_{21} are expected to decrease with increasing temperature, as is typical of ISTs[20].

However, an additional effect needs to be taken into account in our structure. E_{21} decreases at a far greater rate with increasing temperature than does $\hbar\omega_L$, because of the increased electric field required for the higher threshold current density and the large spatial separation of states 2 and 1. As a result, the 2–1 'diagonal' transition shifts to the red, via the linear Stark effect, much more than does the 7–6 'vertical' transition. The net effect is the observed blueshift of the Stokes emission. This behaviour therefore represents additional evidence that the emission at $9\,\mu m$ cannot be due to ordinary laser action. □

Methods

Device

The growth started with a 0.7-μm-thick low n-doped ($n = 5 \times 10^{16}\,cm^{-3}$) GaInAs layer acting as lower waveguide core, on top of which the 30 repetitions of the active region and Raman structure periods (Fig. 1b) were grown. A 0.5 μm GaInAs layer ($n = 5 \times 10^{16}\,cm^{-3}$) completes the waveguide core, on top of which an AlInAs cladding layer was grown with a total thickness of 2 μm, where the first 1 μm was doped to $n = 1 \times 10^{17}\,cm^{-3}$, while the rest of it was doped to $n = 5 \times 10^{17}\,cm^{-3}$. The topmost layer was composed of a highly doped ($n = 4 \times 10^{18}\,cm^{-3}$) 0.8-μm-thick GaInAs layer for plasmon enhanced confinement, and a final 0.1-nm-thick GaInAs contact layer Sn-doped to $n = 1 \times 10^{20}\,cm^{-3}$. The material was processed into ridge waveguides 2.5 mm long and 14–20 μm wide, with a 350-nm-thick Si_3N_4 passivating layer on the lateral walls of the ridge and a Ti(30 nm)/Au(300 nm) top contact. A non-alloyed Ge/Au contact was deposited on the back. The samples were indium-soldered on Ni/Au plated copper holders and mounted in a liquid-nitrogen flow cryostat.

Measurements

A Fourier transform infrared spectrometer was used for optical measurements, together with a calibrated room-temperature HgCdTe detector for the optical power–current characterization. To filter out only the pump laser wavelength in order to measure the optical power emitted at the Stokes frequency, a long-wavelength ($\lambda > 7.5\,\mu m$) pass filter was placed along the light path.

1. Boyd, R. W. *Nonlinear Optics* (Academic, New York, 1992).
2. Shen, Y. R. *The Principles of Nonlinear Optics* (John Wiley & Sons, Hoboken, 1984).
3. Pask, H. M. The design and operation of solid-state Raman lasers. *Prog. Quant. Electron.* **27**, 3–56 (2003).
4. Nishizawa, J. & Suto, K. Semiconductor Raman laser. *J. Appl. Phys.* **51**, 2429–2431 (1980).
5. Grabtchikov, A. S. *et al.* All solid-state diode-pumped Raman laser with self-frequency conversion. *Appl. Phys. Lett.* **75**, 3742–3744 (1999).
6. Liu, H. C. *et al.* Intersubband Raman laser. *Appl. Phys. Lett.* **78**, 3580–3582 (2001).
7. Liu, H. C. *et al.* Coupled electron-phonon modes in optically pumped resonant intersubband lasers. *Phys. Rev. Lett.* **90**, 077402 (2003).
8. Spillane, S. M., Kippenberg, T. J. & Vahala, L. J. Ultralow-threshold Raman laser using a spherical dielectric microcavity. *Nature* **415**, 621–623 (2002).
9. Capasso, F., Sirtorí, C. & Cho, A. Y. Coupled quantum well semiconductors with giant electric field tunable nonlinear optical properties in the infrared. *IEEE J. Quant. Electron.* **30**, 1313–1326 (1994).
10. Rosencher, E. *et al.* Quantum engineering of optical nonlinearities. *Science* **271**, 168–173 (1996).
11. Owschimikow, N. *et al.* Resonant second-order nonlinear optical processes in quantum cascade lasers. *Phys. Rev. Lett.* **90**, 043902 (2003).
12. Gmachl, C. *et al.* Optimized second-harmonic generation in quantum cascade lasers. *IEEE J. Quant. Electron.* **39**, 1345–1355 (2003).
13. Bengloan, J.-Y. *et al.* Intracavity sum-frequency generation in GaAs quantum cascade lasers. *Appl. Phys. Lett.* **84**, 2019–2021 (2004).
14. Khurgin, J. B., Sun, G., Friedman, L. R. & Soref, R. A. Comparative analysis of optically pumped intersubband lasers and intersubband Raman oscillators. *J. Appl. Phys.* **78**, 7398–7400 (1995).
15. Faist, J., Hofstetter, D., Beck, M. & Aellen, T. Bound-to-continuum and two-phonon resonance, quantum-cascade lasers for high duty cycle, high-temperature operation. *IEEE J. Quant. Electron.* **38**, 533–546 (2002).
16. Capasso, F. *et al.* New frontiers in quantum cascade lasers and applications. *IEEE J. Select. Topics Quant. Electron.* **6**, 931–947 (2000).
17. Belyanin, A. A., Bentley, C., Capasso, F., Kocharovskaya, O. & Scully, M. O. Inversionless lasing with self-generated driving field. *Phys. Rev. A* **64**, 013814 (2001).
18. Kocharovskaya, O., Rostovtsev, Yu. V. & Imamoglu, A. Inversionless amplification in the three-level atoms with and without a hidden inversion in reservoir. *Phys. Rev. A* **58**, 649–654 (1998).
19. Gmachl, C. *et al.* Dependence of the device performance on the number of stages in quantum-cascade lasers. *IEEE J. Select. Topics Quant. Electron.* **5**, 808–816 (1999).
20. Helm, M. in *Intersubband Transitions in Quantum Wells: Physics and Applications I* (eds Liu, H. C. & Capasso, F.) 1–91 (Academic, London, 2000).

Correspondence and requests for materials should be addressed to M.T. (troccoli@deas.harvard.edu) or A. B. (belyanin@jewel.tamu.edu).

....

Quantum chemical calculations show that the uranium molecule U₂ has a quintuple bond

Laura Gagliardi[*] & **Björn O. Roos**[*]

Dipartimento di Chimica Fisica "F. Accascina", Universita' degli Studi di Palermo, Viale delle Scienze – Parco d'Orleans II, I-90128 Palermo, Italy, and Department of Theoretical Chemistry, Chemical Center, POB 124, S-221 00 Lund, Sweden

[*] These authors contributed equally to this work

....

Covalent bonding is commonly described by Lewis's theory[1], with an electron pair shared between two atoms constituting one full bond. Beginning with the valence bond description[2] for the hydrogen molecule, quantum chemists have further explored the fundamental nature of the chemical bond for atoms throughout the periodic table, confirming that most molecules are indeed held together by one electron pair for each bond. But more complex binding may occur when large numbers of atomic orbitals can participate in bond formation. Such behaviour is common with transition metals. When involving heavy actinide elements, metal–metal bonds might prove particularly complicated. To date, evidence for actinide–actinide bonds is restricted to the matrix-isolation[3] of uranium hydrides, including H_2U–UH_2, and the gas-phase detection[4] and preliminary theoretical study[5] of the uranium molecule, U₂. Here we report quantum chemical calculations on U₂, showing that, although the strength of the U₂ bond is comparable to that of other multiple bonds between transition metals, the bonding pattern is unique. We find that the molecule contains three electron-pair bonds and four one-electron bonds (that is, 10 bonding electrons, corresponding to a quintuple bond), and two ferromagnetically coupled electrons localized on one U atom each—so all known covalent bonding types are contributing.

Multiple chemical bonds between transition metals were unknown to inorganic chemists until the crystal structure of $K_2[Re_2Cl_8] \cdot 2H_2O$ was reported[6] in 1965. A surprisingly short Re–Re distance of 2.24 Å was found, and assigned to a quadruple bond between the two rhenium atoms. Since then, hundreds of metal–metal multiple bonds have been characterized[7]. Here we extend the concept of metal–metal multiple bonding to the case of two actinide atoms.

The uranium atom (atomic number 92) has the ground-state electronic configuration $(5f)^3(6d)^1(7s)^2$, corresponding to a quintet ground state. However, the energy cost of unpairing the $7s$ electrons by forming hybrid orbitals is minimal, and uranium thus has in principle six electrons available with which to form chemical bonds. In a Lewis-like formalism, these electrons would combine as electron-pair bonds, giving rise to a hextuple bond between the two atoms and a singlet ground state. Such behaviour is seen with the chromium dimer[8], where the six valence electrons reside in the $3d$ and $4s$ orbitals of the Cr atom.

But whereas the Cr atom has exactly one valence electron in each of its six valence orbitals (the five $3d$ and one $4s$ orbitals), the U atom has 16 orbitals (seven $5f$, five $6d$, one $7s$ and three $7p$) that are energetically close to one another. The bonding situation involving uranium is thus considerably more complex, given that all 16 orbitals may be considered valence orbitals available for forming the chemical bond in U₂. This complexity makes simple inferences regarding the nature and strength of the U₂ bond impossible, despite the fact that the strength of a covalent bond depends only on the energy of the atomic orbitals on the two different centres involved, and on the overlap between the orbitals. In the case of U₂, overlap between two $7s$ orbitals and between three out of the five $6d$